

Journal of Stress Analysis

Vol. 8, No. 2, 2023-24, 73-87



ORIGINAL RESEARCH PAPER

Design and Development of a Protection System Combining a Perforated Plate and Lightweight Composite Armor against 12.7mm Caliber Threats

Hamad Rajab[®], Ali Davar[®], Tayebeh Akbari[®], Jafar Eskandari Jam[®] Faculty of Materials & Manufacturing Technologies, Malek-e Ashtar University of Technology, Tehran, Iran.

Article info

Article history: Received 15 February 2024 Received in revised form 11 March 2024 Accepted 19 March 2024

Keywords: Armor piercing Perforated steel plate Asymmetric impact Conical holes

Abstract

This study examines the ballistic behavior designed and developed to protect against lightweight composite armor for large-caliber 12.7mm armor-piercing (AP) threats. To achieve this, a perforated steel plate combined with a base armor (SiC-Kevlar) is utilized. The efficient selection of materials and optimized design are key to attaining lightweight armor. Accordingly, the most suitable materials in the best geometric configuration are identified for each component of the system. Based on the selected material, a novel geometric design for the perforated plate's holes was proposed, replacing the traditional cylindrical holes with conical ones. The proposed design simultaneously ensures greater potential for asymmetric impact and structural integrity of the armor structure, thereby improving its ballistic performance. Finite element simulations using LS-DYNA, along with the response surface method (RSM), were employed to optimize key parameters of the perforated plate, such as cone angle and air spacing. The results suggest that the proposed conically perforated plate design can be more effectively utilized than the cylindrical perforated plate for ballistic protection, regardless of whether the impact occurs at the center of the hole or at its edge.

Nomenclature

AP	Armor-Piercing	FEM	Finite Element Method
P	Represents the pressure	σ_0	Flow stress
γ_0	Grüneisen coefficient	ρ_0	Initial density of the material
E	The absolute internal energy	$\mid \mu \mid$	Specific volume
G	Shear modulus	β	Bulking factor
ε_P	Equivalent plastic strain	$\frac{\dot{\varepsilon}_P}{\dot{\varepsilon}_0}$	The dimensionless plastic strain rate
T_m	Temperature melting	$\begin{array}{c c} \frac{\dot{\varepsilon}_P}{\dot{\varepsilon}_0} \\ T_r \end{array}$	Reference temperatures
m	The thermal softening coefficient	C_p	Specific heat
D	Scalar damage variable	R	Diameter of hole
σ^*	The normalized equivalent stress	HEL	Hugoniot Elastic Limit
σ_i^*	Equivalent strength of intact ceramic	YC	Transverse compressive strength, b-axis
ε_p^f	Failure strain	N	Intact strength constant

^{*}Corresponding author: A. Davar (Assistant Professor)

E-mail address: davar78@gmail.com doi 10.22084/JRSTAN.2024.28243.1248 ISSN: 2588-2597





K_1	Bulk modulus	K_2, K_3	Pressure constant
AOPT	Material axes option	RO	Mass density
EA	Young's modulus in a-direction	EB	Young's modulus in b-direction
EC	Young's modulus in c-direction	PRBA	Poisson's ratio, ba.
PRCA	Poisson's ratio, ca.	PRCB	Poisson's ratio, cb.
GAB	Shear modulus, ab.	GBC	Shear modulus, bc.
GCA	Shear modulus, ca.	KFAIL	Bulk modulus of failed material
SC	Shear strength, ab plane		Normal tensile strength
SYZ	Transverse shear strength	SZX	Transverse shear strength
XT	Longitudinal tensile strength, a-axis	YT	Transverse tensile strength, b-axis
ρ	The immediate density of the material	MACF	Material axes change flag for brick ele-
	under hydrostatic compression		ments
$S_1, S_2,$	The slant coefficients of the particle ve-	P_n	The probability of projectile fragmen-
S_3	locity - shock velocity relationship		tation
A, B,	Johnson Cook material constants	$D_1, D_2,$	JC fracture strain model constants
n, m,		$D_3, D_4,$	
C		D_5	
σ_f^*	Equivalent strength of fractured ce-		
	ramic		

1. Introduction

The development of protection systems against fragments and large- and small-caliber projectiles is a crucial area of research for both civilian and military applications. The threat posed by automatic weapon fire is particularly critical for vehicles, as multiple projectiles can target a confined area, necessitating the implementation of multi-hit protection [1].

This issue is particularly prominent when brittle materials such as ceramics fail to provide adequate multi-hit protection. Additionally, brittle behavior has been observed in homogeneous metallic armor (e.g., aluminum and steel alloys). Studies have shown that aluminum allovs and steel plates can shatter in a brittle manner upon collision with armor-piercing (AP) projectiles, leading to cracks that compromise multi-hit resistance when mounted as ceramic armor on vehicles. Perforated steel plates present a potentially more effective solution due to their higher flexibility and ability to limit crack propagation from the impact point to the nearest hole. This characteristic preserves a larger portion of the armor compared to ceramics, where an entire tile may be shattered upon impact [2-4]. Cui et al. showed that when a projectile strikes, it either changes its trajectory or fractures into fragments due to bending stress [5]. Also, the optimal design of coating thickness may be necessary to enhance the ballistic resistance of amorphous-alloy-reinforced perforated armor (ARPA). Chocron et al. [6] established the principles of perforated plates, demonstrating that a 7.62mm×51mm M2AP round undergoes bending when impacting the plate edge, requiring a tensile strain of 2%. They demonstrated that the erosion strain of the jacket is a critical parameter for successful simulations. Kilic et al. [7] confirmed the high performance

of perforated plates in the ballistic protection through experiments using the 7.62 armor-piercing and incendiary (API) projectiles. They analyzed the stochastic nature of the ballistic tests on perforated armor plates based on the bullet impact zone with respect to holes. Various scenarios including those with and without bullet failure models were investigated to determine the mechanisms of the bullet failure. Radisavljevic et al. [8] offered a model showing that perforation diameter is crucial for achieving penetration core fragmentation. Smaller perforations cause smaller bending stresses, which result in two effects. The first effect is the induction of bending stresses in the core/plate overlapping area. The second is the stabilizing effect on the opposite side which is smaller if the perforations are larger, causing larger bending stresses and higher penetrating fragmentation of the core.

Mubashar et al. [9] investigated the ballistic response of a newly designed perforated armor plate considering a 12.7mm armor piercing tracer (APT) projectile. Analytical and experimental studies were conducted, and the projectile's penetration through a base aluminum plate (AA5083-H116) is studied considering both the presence and absence of the perforated armor plate. The perforated armor plate was made using 30SiMnCrMoV (550HB) steel. The steel used has high tensile strength and considered as a low-alloy structural steel. As a result, an 8mm thick plate with 9.5mm diameter holes was considered. The study showed that the proposed design of the perforated armor plate and the base armor plate could withstand the 12.7mm AP projectile. Hao et al. [10] investigated how hole arrangement and shape influence the ballistic behavior and failure mode of a perforated structure. Different impact speeds involving three domains of the velocity value, two types of hole arrangements, and three kinds of hole shapes (i.e., square, triangular, and circular) of perforated steel plates are considered to study the projectile deflection effect. By analyzing the numerical and experimental results, the asymmetric ballistic responses were repeatedly highlighted due to the impact that occurs in the area close to the edge of the hole.

Anshun et al. [11] conducted a ballistic test of a 12.7mm piercing shell penetrating different perforated steel plates to evaluate their protective performance of different perforated steel plates. Based on the ballistic test results, the residual penetration depth of different base armors, the damage area of perforated plates, and the number of core fractures were analyzed. The study showed that the projectile deflection angle of perforated plates made of different armor steel materials also followed a linear relationship, and the slope of the fitted line could be used to quantify the degree of core deflection. The higher the hardness of perforated plates with circular holes, the greater the core deflection, while the hexagonal hole configurations caused greater core deflection than circular ones. Acar et al. [12] studied the ballistic impact response of two armor steels (Armox Advance and Ramor 500) and a structural wear-resistant steel (Hardox 450) in monolithic, double-layered, and perforated plate configurations. Ammunition types used in the ballistic tests included 7.62mm NATO Ball, 7.62×51AP, and 12.7mm APM2 bullets. The tests were performed in accordance with EN 1522/1523 ballistic test standards and at FB6 and FB7 levels. The results showed different perforation behaviors for different plate configurations. All the monolithic plates were perforated with 7.62mm AP bullets except for Armox Advance. Double-layered plate configurations, on the other hand, showed resistance to penetration. All the pre-perforated plate configurations resulted in total protection regardless of ammunition type and plate materials, highlighting the effectiveness of perforated plates. Alawsi et al. [13] performed an experimental test by shooting a 2mm steel target (150×150mm) with a 9×19 Parabellum full metal jacket projectiles moving at a ballistic velocity of 370m/s. On the other hand, numerical work was conducted to simulate the same event using LS-DYNA, an explicit finite element code. The objective of this work was to demonstrate the capability of LS-DYNA software in simulating the effects of ballistic impact and analyzing the performance of steel plate armor. The numerical analysis demonstrated that all constitutive models effectively predicted the qualitative behavior of the physical mechanisms during perforation. For practical applications, the suitable selection of the type of constitutive model and criterion of fracture employing the finite element method (FEM) leads to an excellent agreement with the experimental results of projectile impacts on steel targets under the same conditions.

The ballistic performance of the perforated plate depends on the bullet's point of impact, with four main cases identified: (1) the bullet impacts the center of a hole, (2) bullet strikes the hole's side, (3) bullet lands between two holes, or (4) bullet hits the center of three holes. The critical case-when the bullet strikes the hole's center-exhibits reduced ballistic effectiveness, as lateral forces and stress induction do not occur. Conversely, the closer the projectile is to the hole's edge, the greater the ballistic effectiveness [14]. In most cases, additional perforated armor, which relies on ballistic deflection and projectile fracture, is effective when positioned at an optimal distance from the base armor. In such configurations, air spacing is necessary to allow fragment separation, reduce penetration and enable adequate projectile deflection, thereby ensuring that the base armor provides full ballistic protection [15].

In previous studies, the ballistic effectiveness of perforated plates was not evaluated for critical impact conditions, specifically when the projectile strikes the center of the hole-a scenario that significantly reduces the plate's effectiveness. Additionally, limited attention has been given to optimizing the geometric design of the perforations and the air spacing between the perforated plate and the base armor, despite their critical influence on ballistic performance. This study introduces an innovative perforated plate design featuring conical holes instead of conventional cylindrical ones. The conical geometry enhances the probability of asymmetric impact, leading to increased projectile deviation, fragmentation, and energy dissipation. Furthermore, the optimal air spacing is determined using Response Surface Methodology (RSM) to maximize projectile deflection and minimize penetration depth. These advancements bridges existing gaps in the literature and presents a novel lightweight protection system against 12.7mm caliber threats (Fig. 1).

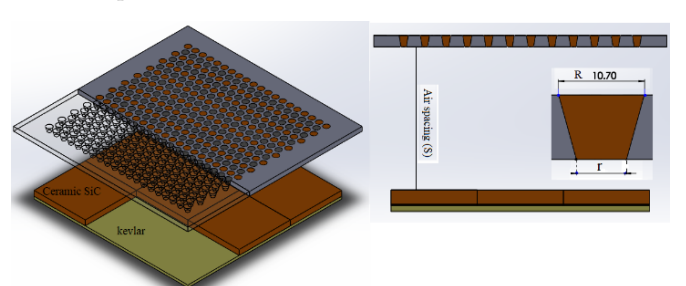


Fig. 1. The configuration of the protection system.

2. Research Materials and Methods

This study employs numerical simulation to design and develop an advanced armor protection system comprising lightweight composite armor (ceramic SiC/Kevlar) and a perforated armor plate made of Armox 500T to counter 12.7mm caliber threats. The armor configuration consists of a 10mm ceramic layer, a 4.6mm Kevlar backing, and an 8mm perforated plate. The perforated plate features a conical hole pattern arranged in a dislocated configuration. RSM is utilized to optimize key geometrical parameters, including the conical hole slope and the optimal air spacing.

2.1. Numerical Simulations

In this work, LS-DYNA software is used to numerically analyze the ballistic response of the perforated armor plate. The high-velocity impacts on the perforated steel plate are simulated using a numerical model that incorporates rapid changes in pressure, temperature, density, and total internal energy [16]. The equation of state (EOS) is a fundamental thermodynamic relationship that characterizes a material's pressure, temperature, and density. In this context, the Mie-Grüneisen EOS models were applied to both the perforated plate and the projectile to capture the pressure and shock wave dynamics within the numerical simulations. The pressure P in the Mie-Grüneisen EOS model [17], under compression, can be written as:

$$P = \begin{cases} \frac{\rho_0 C_0^2 \mu \left[1 + \left(1 - \frac{\gamma_0}{2} \right) u - \frac{a}{2} \mu^2 \right]}{\left[1 - (S_1 - 1)\mu - S_2 \frac{\mu^2}{\mu + 1} - S_3 \frac{\mu^3}{(\mu + 1)^2} \right]^2} + (\gamma_0 + a \ \mu) E \\ (\mu \ge 0) \\ \rho_0 C_0^2 \mu + (\gamma_0 + a \ \mu) E \\ (\mu < 0) \end{cases}$$

where ρ_0 is the initial density, ρ is the instantaneous density of the material under hydrostatic pressure, μ

is a specific volume term given by $\mu = \rho/\rho_0 - 1$, γ_0 is Grüneisen coefficient, a is the first order volume correction factor to γ_0 , C_0 is the Hugoniot intercept of the shock velocity and particle velocity curve. Also, S_1 , S_2 , and S_3 are the slope parameters of the particle velocity —shock velocity curves, whereas E is the absolute internal energy. The parameters related to the Mie-Grüneisen EOS model are shown in Table 1.

Table 1
Mie-Gruneisen EOS parameters for both perforated plate and the projectile [16].

Material	$C_0 (\mathrm{m/s})$	S_1	S_2	S_3	γ_0
Projectile core	4570	1.49	0	0	1.93
Steel Armox 500T	4570	1.49	0	0	1.93

For problems with high strain and large deformations, the strain-rate-sensitive Johnson-Cook (J-C) model is used to simulate compressive strength [18]. This model incorporates failure criteria, strain rate effects with increasing strength, damage effects and thermal effects [10]. In the mentioned model, the dynamic Von-Mises flow stress is given by [19]:

$$\sigma_0 = (A + B \, \varepsilon_P^n) \left(1 + C \ln \frac{\dot{\varepsilon}_P}{\dot{\varepsilon}_0} \right) \left[1 - \left(\frac{T - T_r}{T_m - T_r} \right)^m \right]$$
(2)

Where, ε_P is the plastic strain, and $\dot{\varepsilon}_P$ is the plastic strain rate, and $\dot{\varepsilon}_0$ is the reference strain rate. Additionally, A is the quasi-static yield strength of the unstrained material, B is the hardening coefficient, n is the strain hardening exponent. C is the strain rate hardening constant. Also, T_m is the melting temperature, T_r is the reference temperatures, and finally, the softening exponent is denoted by m. The parameters of the J-C plasticity model are Presented in Table 2.

Table 2
Parameters of the materials used for the projectile and armor plates [19].

Parameter	Symbol	Unit	Al 5083-H116	Projectile core	Perforated plate			
				Steel 4340	Steel Armox 500T			
Density	ho	(g/cm^3)	2700	7850	7850			
Shear modulus	G	GPa	26.4	80	75.6			
Specific heat	C_p	J/kg K	910	477	455			
Johnson-Cook plasticity model parameters								
Initial yield stress	A	MPa	167	1900	1372.5			
Strain hardening coefficient	B	MPa	596	1100	835			
Strain hardening exponent	n		0.551	0.3	0.2467			
Thermal softening exponent	m		0.859	1	0.84			
Melting temperature	T_m	K	893	1800	1800			
Reference temperature	T_r	K	293	300	293			
Strain rate coefficient	C		0.001	0.05	0.0617			
Reference strain rate	$\dot{arepsilon}_0$	1/s	1	0.001	1			

The J-C damage model can be stated as [20]:

$$\varepsilon_f = [D_1 + D_2 \exp(D_3 \sigma^*)] \left(1 + D_4 \ln \frac{\dot{\varepsilon}_P}{\dot{\varepsilon}_0} \right)$$

$$(1 + D_5 T^*)$$
(3)

where ε_f is the failure strain, D_1 - D_5 are the material parameters, and $\sigma^* = \sigma_m/\sigma_{eff}$ is the ratio of the mean pressure (σ_m) to the equivalent Von-Mises stress (σ_{eff}) . The J-C damage model parameters are given in Table 3.

Table 3The J-C damage model parameters for the projectile core and armor plates [19, 20].

Material	D_1	D_2	D_3	D_4	D_5	
Steel Armox	0.04280	9 1591	2 7575	-0.0066	0.86	
500T	0.04269	2.1921	-2.1313	-0.0000	0.80	
Projectile core	0.05	3.44	-2.12	0.002	0.61	
Steel 4340	0.05	3.44	-2.12	0.002	0.01	
Al 5083-H116	0.0261	0.263	-0.349	0.147	1.68	

The ceramic model of Johnson–Holmquist (MAT_110) [21] is used to simulate the behavior of silicon carbide ceramic. Table 4 lists the parameters associated with this model [22] where the equivalent stress can be expressed in normalized form as:

$$\sigma^* = \sigma_i^* - D\left(\sigma_i^* - \sigma_f^*\right) \tag{4}$$

The normalization is performed using the equivalent stress at the Hugoniot elastic limit, rendering the stress dimensionless. It can then be written as:

$$\sigma^* = \sigma / \sigma_{HEL} \tag{5}$$

The equation that defines the normalized equivalent strength of intact ceramic (σ_i^*) is:

$$\sigma_i^* = A(P^* + T^*)^N \left[1 + C \ln \left(\dot{\varepsilon} / \dot{\varepsilon}_0 \right) \right]$$
 (6)

while the normalized equivalent strength of fractured ceramic (σ_f^*) can be calculated using the following equation:

$$\sigma_f^* = B(P^*)^M \left[1 + C \ln \left(\dot{\varepsilon} / \dot{\varepsilon}_0 \right) \right] \tag{7}$$

of incremental plastic deformation (ε_P) :

The accumulated damage is expressed as a function

$$D = \sum \frac{\Delta \varepsilon_P}{\Delta \varepsilon_P^f} \tag{8}$$

$$\varepsilon_p^f = D_1 (P^* + T^*)^{D_2} \tag{9}$$

where $\Delta \varepsilon_P$ is the incremental effective plastic strain, $\Delta \varepsilon_P^f$ is the failure strain, and D_1 and D_2 are material constants. Also, A, B, C, M, and N are constants related to the material, and D represents the damage factor which ranges between 0 and 1.

The pressure model can be written as:

$$P = K_1 \mu + K_2 \mu^2 + K_3 \mu^3 + \Delta P, \tag{10}$$

where K_1 , K_2 , and K_3 are constants, and μ is the compressibility factor. To get rid of the distorted elements of the ceramic, the instantaneous geometric strain metric is considered. In this work, the erosion strain is set to 1.5.

To model the Kevlar fiber, the MAT_ 22 model is applied using the composite damage by using a set of orthotropic constitutive relations is considered to define the relationship between stress and strain. In that model, the failure modes are categorized into four categories: the first and second deals with tensile failure and compressive failure of matrix whereas the third and fourth deals with tensile failure and compressive failure of fibers. The associated material parameters are listed in Table 5.

The geometrical model and the dimensions of the projectile are clearly depicted in Fig. 2. The projectile material is considered to be steel 4340 with an initial incident velocity of 820m/s. Taking into consideration the symmetry of the perforated plate and the projectile, only a half-model was built to reduce the computation. The perforated plate was meshed with a solid mesher in two different zones: bullet contact and outer zone. The mesh size increases in radial direction from the projectile contact zone to the outer zone and varies between 0.7 and 1.9mm in size. The projectile was meshed with a solid Mesher with an element size of 0.6mm (See Fig.3).

Table 4
The JH-2 model constants and material for SiC [22].

Parameters	Value	Parameters	Value
Density, ρ (g/cm ³)	3.18	Strain rate constant, C	0.0045
Bulk modulus, K_1 (GPa)	217.2	Fracture strength constant, B	0.35
Pressure constant, K_2 (GPa)	0.0	Fracture strength exponent, M	1.0
Pressure constant, K_3 (GPa)	0.0	Maximum fracture strength ratio	1.0
Bulking factor, β	1.0	Hydro tensile limit, T (GPa)	-0.75
Shear modulus, G (GPa)	183.8	Damage constant, D_1	0.48
Hugoniot elastic limit (HEL) (GPa)	14.7	Damage constant, D_2	0.48
Intact strength constant, A	0.96	Intact strength constant, N	0.65

Table 5
The parameters of Kevlar Ortho model [22].

Parameters	$\rho (\mathrm{kg/m^3})$	EA (GPa)	EB(GPa)	EC (GPa)	PRBA	PRCA	PRCB	GAB (GPa)
Kevlar	1440	35	35	8.33	0.0045	0.044	0.044	0.35
Parameters	GBC (GPa)	GCA (GPa)	Alph	Kfail (GPa)	Aopt	Macf	Sc(GPa)	Xt (GPa)
Kevlar	0.32	0.32	0	2.2	1.0	3	0.025	0.725
Parameters	Yt (GPa)	Yc (GPa)	$\operatorname{Sn}\left(\operatorname{GPa}\right)$	Syz (GPa)	Szx (GPa)	-	-	-
Kevlar	0.725	0.69	9.0	1.08	1.8	-	-	-

The multilayer ceramic-Kevlar/epoxy composite consists of two different layers, the first is the ceramic layer which consists of Silicon carbide whereas the second layer is Kevlar/epoxy composite layer. The dimensions of the plates are considered as 300mm×300mm. In the finite element analysis, the element size through the thickness direction is 0.7mm and this element dimension is also considered for the central region (13mm×13mm) but this value is increased gradually as it gets far from the plate center. The four edge faces of the plate are considered fixed, with zero displacement and rotation values assigned (See Fig. 4). The eroding surface-to-surface contact is also simulated among the different parts (perforated plate, projectile, multilayer ceramic-Kevlar/epoxy). A zero-velocity boundary condition is considered for the four vertices of the perforated plate.

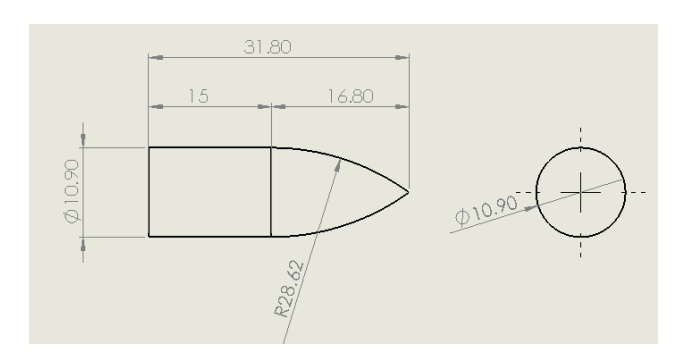


Fig. 2. Projectile size (mm).

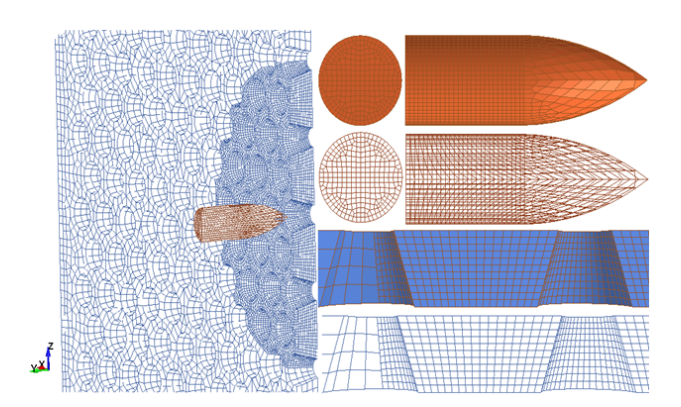


Fig. 3. The model of the projectile and the perforated plate.

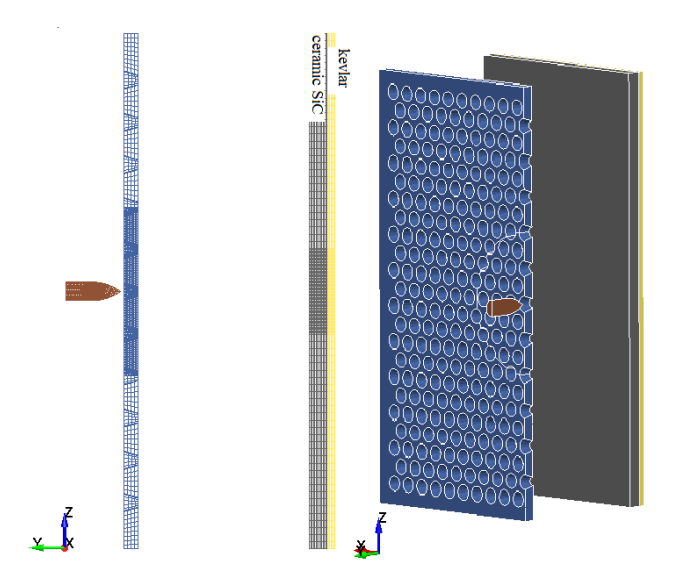


Fig. 4. Configuration of projectile and target plate (perforated plate/ceramic/Kevlar).

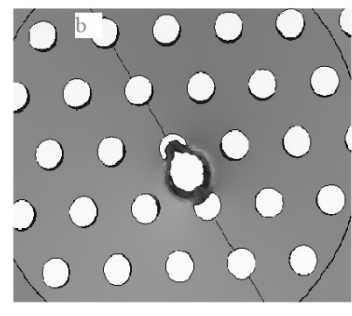
2.2. Verification of LS-Dyna Model

This section verifies the accuracy of the current LS-Dyna model by comparing its simulation results with both the experimental and simulation data from Mubashar et al. [9]. A finite element (FE) model for the projectile and the perforated plate made from Armox 500T steel, 8mm thickness, a diameter of hole 9mm, and base armor made from 38.1mm thick aluminum AA5083-H116 was created, and the results are compared with the experimental data shown by Mubashar et al. [9]. The accuracy of the current simulations is assessed based on the details of the projectile's impact and residual velocities provided in Table 6. There is also a strong correlation between the size and shape of the damaged areas reported in Ref. [9] and those obtained from the current numerical simulation. The simulation results, both in terms of residual velocity and depth of penetration, demonstrate consistency with the experimental results. The present simulation accurately shows the Penetration process of the 12.7mm projectile, the proposed perforated steel plate, and the aluminum plate, consistent with the actual test results reported by Mubashar et al. [9], as depicted in Fig. 5 for Al 5083-H116 plate and Fig. 6 for perforated plate+ Al 5083-H116 plates.

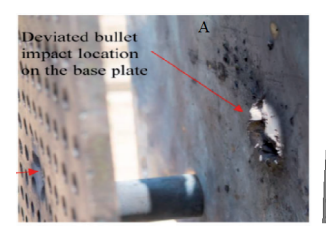
Table 6									
The simulation	results ar	nd those	reported	by	Mubashar	$_{ m et}$	al.	[9].	

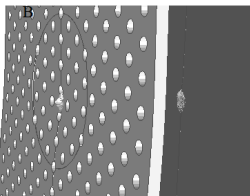
		Residual velocity	Residual velocity	DOP	DOP	
Initial velocity	Configuration	(simulation,	(present	(simulation,	(present	% Error
(m/s)	of target	Mubashar et al.)	simulation)	Mubashar et al.)	simulation)	/0 E1101
		(m/s)	(m/s)	(mm)	(mm)	
864	Al 5083-H116	514.3	555	Penetration	Penetration	7.3
864	Perforated plate	0	0	10.46	10.8	3.1
004	+ Al 5083-H116	U	0	10.40	10.6	3.1





a) Notch formation in experiment [9] and b) Notch formation in the present finite element (FE) model.





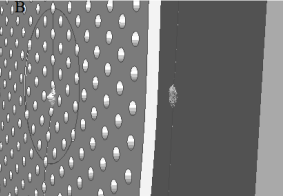


Fig. 6. a) Notch formation in the experiment (perforated/Al) [9] and b) Notch formation in the present finite element (FE) model.

3. Results and Discussion

Initially, the impact of the 12.7mm projectile on the perforated plate and base armor (aluminum) was simulated using the commercial finite element (FE) code LS-DYNA to validate the model (Fig. 6). The simulation aimed to assess the effectiveness of the proposed perforated plate geometry. When the projectile struck the center of a hole (the critical case), its velocity decreased from 820m/s to 557m/s. Additionally, a numerical study was conducted to evaluate the ballistic performance of each component of the protection system and its contribution to stopping the projectile.

3.1. Perforated Plate Geometry

The hole patterns were developed based on a theoretical analysis of a probabilistic model [23], which facilitated the identification of optimal perforation parameters. These perforated steel plates are designed to generate bending stresses destabilizing the projectile, leading to its fragmentation and decreasing its penetrating capability. The base armor subsequently intercepts the resulting fragments. The core concept of the statistical model is to identify the ideal arrangement of holes and their spacing to get the maximum weight reduction while maintaining or enhancing the protective efficiency. This model operates on the premise that bending stress is created when the projectile impacts both inside the hole and in a specific area outside, a phenomenon explained by the edge effect principles. A set of parameters are considered to describe the perforated plate, such as the hole diameter (R) and the distance between any two centers of adjacent holes (T). In addition, two surface areas are defined: the first surface area with a width of (δ) is where deflection or fragmentation is likely to occur, the second is the surface where the penetration could happen without a deflection. The previous parameters are depicted in (Fig. 7).

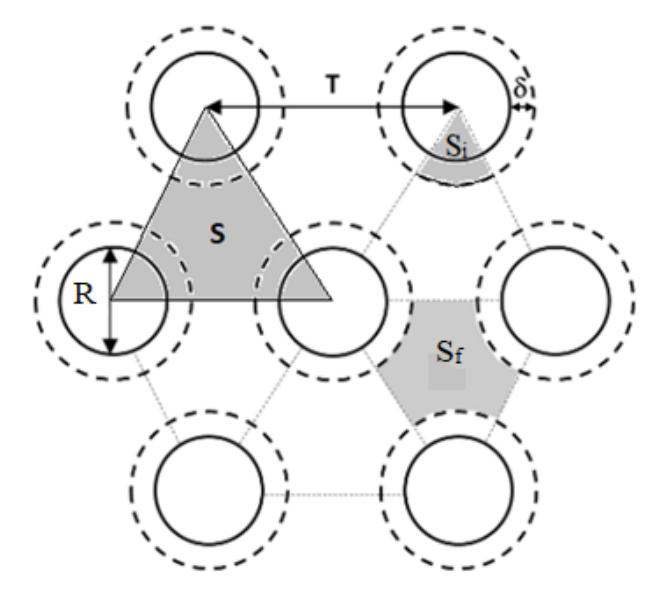


Fig. 7. The pattern of the perforation diagram with a 60° Stagger.

The first step in calculating the perforation layout was to determine the value of δ . This value was obtained using a formula by applying the conditions that give rise to the edge effect [23].

$$\delta/\frac{D}{2} \ge 0.35 \tag{11}$$

where D represents the diameter of the projectile core, and δ is the width of the overlap area described above.

$$\delta \ge 0.35 \left(\frac{D}{2}\right)$$

$$\delta \ge 0.35 \left(\frac{10.9}{2}\right) \quad \Rightarrow \quad \delta = 1.9 \text{mm}$$

$$(12)$$

The diameter R shown in Fig. 7 is then calculated as follows:

$$\delta = D - R \Rightarrow R = D - \delta = 10.9 - 1.9 = 9 \text{mm}$$

When the diameter of the perforation hole approaches that of the penetrator, the surface area stabilizing the projectile penetrator is significantly decreased. Meanwhile, the surface area contributing to the penetrator bending stress remains constant (Fig. 8) [23]. The optimum value of the hole diameter (R_{opt}) is obtained as D - 0.2. So, the R_{opt} for the 10.9mm diameter projectile penetrator is 10.7mm. After that, the variance range of the perforation pattern T is determined, then its optimal value T_{opt} was determined according to Eq. (14) and Eq. (15), with the assumption that the failure probability of projectile penetration in the first shot is 0.95. The surface area that leads to projectile penetrator fragmentation (S_i) was calculated using Eq. (13):

$$S_i = 0.5 * \pi \left(\frac{R}{2} + \delta\right)^2 \tag{13}$$

The probability of projectile fragmentation (failure), denoted as P_n , for the first shot was calculated as follows:

$$P_n\left(1\right) = \left(\frac{S_i}{S}\right) \tag{14}$$

$$S = \frac{T^2 * \sqrt{3}}{4} \tag{15}$$

(17)

Where, S represents the surface area between the centers of three adjacent holes.

$$P_n(1) = \left(\frac{S_i}{S}\right) = \frac{2 * \pi \left(\frac{R}{2} + \delta\right)^2}{T^2 * \sqrt{3}}$$

$$T_{opt} = \sqrt{\frac{2 * \pi \left(\frac{R_{opt}}{2} + \delta\right)^2}{P_n(1) * \sqrt{3}}}$$

$$(16)$$

$$T_{opt} = \sqrt{\frac{2 * \pi (5.35 + 1.9)^2}{0.95 * \sqrt{3}}} = 14.2 \text{mm}$$

$$S_i = 0.5*\pi \left(\frac{10.7}{2} + 1.9\right)^2 = 82.7 \text{mm}^2$$

$$S = \frac{14.2^2 * \sqrt{3}}{4} = 87.3 \text{mm}^2$$

$$S_f = S - S_i = 4.6 \text{mm}^2$$

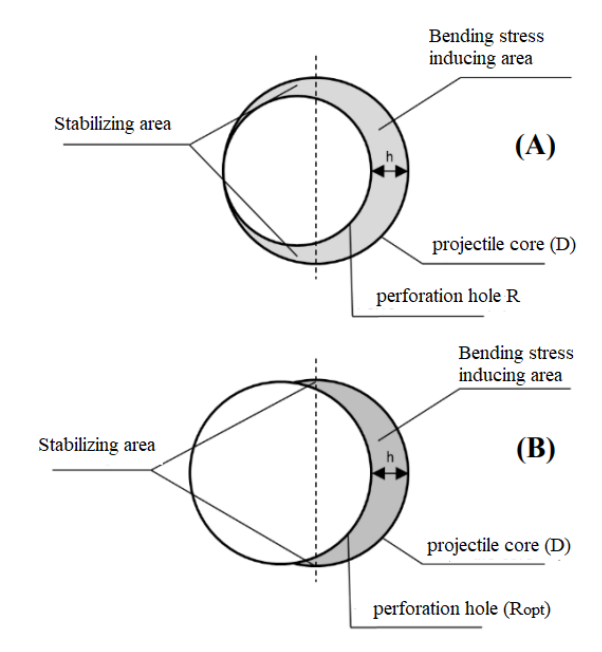


Fig. 8. Optimization of Hole Diameter in Perforated Steel Plate Diagram [23].

The geometric configuration of the perforated plate is shown in (Fig. 9). In this figure, the probability of asymmetric impact that ensures the projectile deflection is 0.95. Based on previous studies, the initial evaluation of the perforated plate's ballistic performance is as follows: This design provides the highest possibility of asymmetric impact. However, the bending stresses generated are insufficient to fragment the projectile core. Here, the residual velocity is high due to the low structural strength of the perforated plate. Additionally, the ballistic protection of the perforated plate is almost non-existent when the impact point is at the center of the hole. The ballistic effectiveness was improved, and the highest possibility of asymmetric impact was ensured simultaneously using conical holes instead of cylindrical ones (Fig.10). A numerical study of the proposed model (conical holes) was conducted in addition to the application of the design of experiments (DOEs) methods (RSM) to determine the optimal cone angle that provides the best ballistic protection and the lowest weight of the perforated plate.

3.2. Optimization of the Geometry of the Conical Hole and Air Spacing

To optimize the protection system design, RSM was employed according to Table 7 to determine the optimal geometric parameters, including the minor cone circle diameter (r) and the air spacing between the perforated plate and the base armor (S), which are introduced as design variables introduced in Table 8.

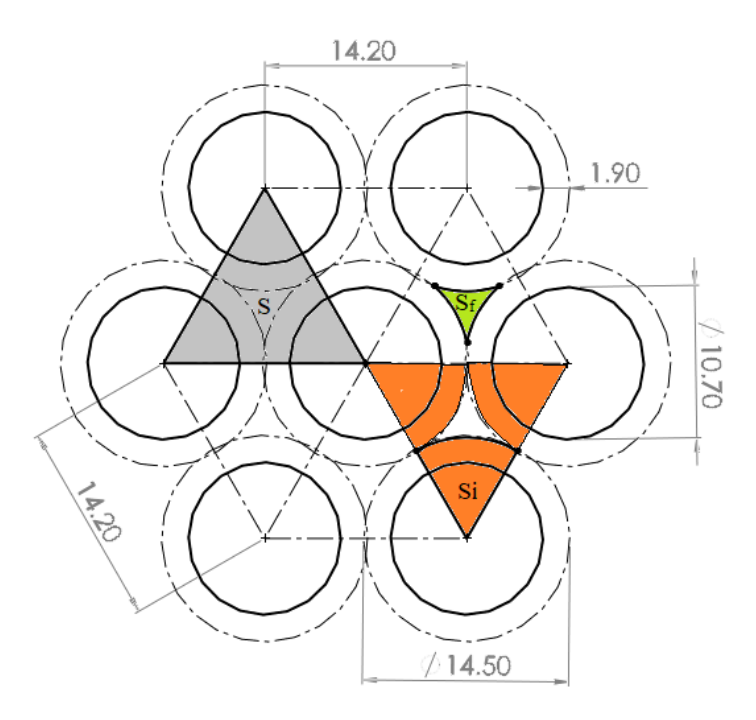


Fig. 9. The geometric configuration of the perforated plate.

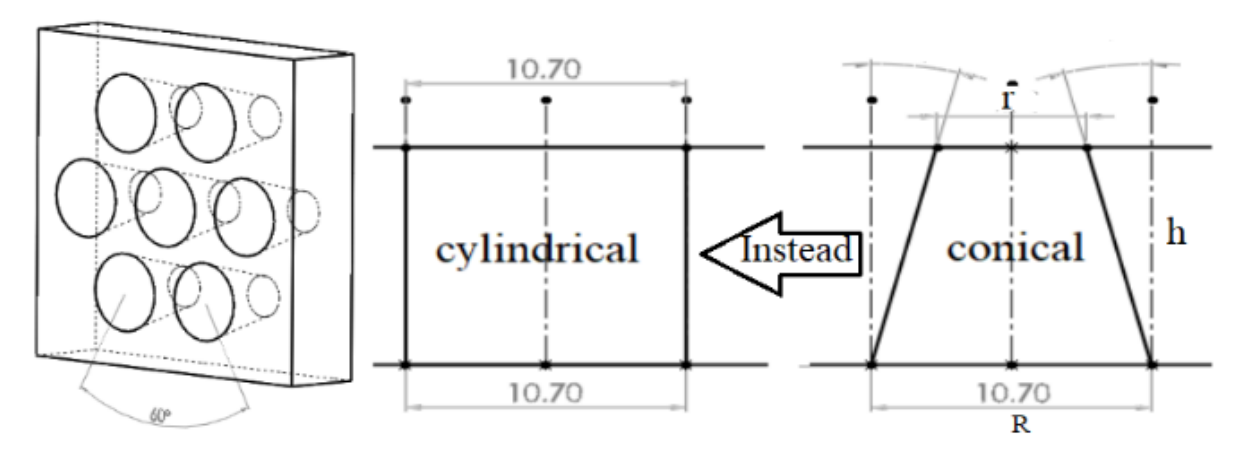


Fig. 10. Geometry of conical frustum (hole).

Table 7 RSM build information.

File version	13.0.5.0			
Study type	Response surface		${\bf Subtype}$	Randomized
Design type	I-optimal	Coordinate exchange	Runs	14.00
Design model	Quadratic		Blocks	No Blocks
Build time (ms)	6.00			

 Table 8

 Optimization factors information (design variables).

Factor	Nama	Units	Type	SubType	Minimum	Maximum	Coded	Coded	Mean	Dev.
	rvame						Low	High	Mean	Std.
A	A (r)	mm	Numeric	Discrete	6.00	10.70	$-1 \leftrightarrow 6.00$	$+1 \leftrightarrow 10.70$	8.36	1.64
В	B (S)	mm	Numeric	Discrete	50.00	250.00	$-1 \leftrightarrow 50.00$	$+1 \leftrightarrow 250.00$	146.43	66.40

The designed experiments were modeled to optimize ballistic performance by minimizing the projectile's residual velocity, reducing the weight of the perforated plate, and decreasing the depth of penetration in the base armor. Additionally, the objective was to minimize the internal energy absorbed by the base armor to effectively stop the projectile, as well as to reduce the total thickness of the armor system as shown in Table 9.

The design of experiment setup is detailed in Table 10, where two key parameters-the minor cone circle diameter (r) and air spacing (S)-were systematically varied. Five critical responses were evaluated: (1) residual velocity of the projectile, (2) total weight of the armor system, (3) penetration depth in the base armor, (4) internal energy absorption by the base armor, and (5) total thickness of the armor system. Numerical simulations were performed using LS-DYNA across multiple scenarios to compute these responses where the impact point is at the edge of a hole. The results are summarized in Table 10. The advantages of the newly designed conical holes over traditional cylindri-

cal holes become more evident when comparing run no. 5 (r=6mm) and run no. 14 (r=10.7mm). In these instances, for example, for the same air spacing value (S=150mm), there is approximately 26% more weight, about 35% less residual velocity, about 72% less depth of penetration, and about 64% less internal energy of the base armor. These results are highly advantageous for large caliber AP protection systems. Further investigation revealed that in a similar scenario, when the projectile strikes the center of a hole, there is approximately 31% less residual velocity. Therefore, the proposed conically perforated plate design could be utilized more effectively than the cylindrical perforated plate for ballistic protection, regardless of whether the impact occurs at the center of the hole or at its edge.

The final RSM step involved analyzing the data obtained using the I-Optimal design approach to determine the optimal values for the minor cone circle diameter (r_{opt}) and air spacing (S_{opt}) . The numerical analysis revealed that the optimal design parameters were $r_{opt} \approx 6$ mm and $S_{opt} \approx 170$ mm according to Table 11, as illustrated in Fig. 11.

Table 9
Responses information (multi-objective functions).

	1	\		,					
Ī	Response	Name	Units	Observations	Minimum	Maximum	Mean	Std. Dev.	S/N Ratio
_	R1	R1 (R-velocity)	m/sec	14.00	397	617	561.93	74.86	1.55
	R2	R2 (DOP)	mm	14.00	1.4	19.3	7.04	4.34	13.79
	R3	R3 (I-energy)	J	14.00	53.6	322	158.26	72.57	6.01
	R4	R4 (Weight)	g	14.00	3280	4120	3690.00	306.52	1.26
	R5	R5 (Total Thickness)	$\overline{\mathrm{mm}}$	14.00	72.6	272.6	169.03	66.40	3.75

Table 10
The (actual) design by the design of experiments (RSM- I-optimal).

	Factor 1	Factor 2	Response 1	Response 2	Response 3	Response 4	Response 5
Run	A (r)	B (S)	R1 (R-velocity)	R2 (DOP)	R3 (I-energy)	R4 (Weight)	R5 (Total Thickness)
	$\overline{\mathrm{mm}}$	$\overline{\mathrm{mm}}$	m/sec	mm	J	g	mm
hline 1	9	150	595	6.4	137	3540	172.6
2	9	150	595	6	137	3540	172.6
3	9	50	595	8.4	227	3540	72.6
4	10.7	50	610	19.3	322	3280	72.6
5	6	150	397	2.1	57	4120	172.6
6	8	100	617	11.4	209	3740	122.6
7	9	150	595	6.4	137	3540	172.6
8	10.7	200	610	5.4	173	3280	222.6
9	7	250	543	5.1	119	3980	272.6
10	8	200	617	6.4	127	3740	222.6
11	6	150	397	1.4	53.6	4120	172.6
12	7	50	543	8.4	243	3980	72.6
13	7	250	543	4.4	115	3980	272.6
14	10.7	150	610	7.4	159	3280	172.6

Table 11 Optimal numerical solutions of r_{opt} (minor cone circle diameter) and S_{opt} (air spacing).

Number	A	В	R1	R2	R3	R4	R5	Desirability	
	(\mathbf{r}_{opt})	(S_{opt})	(R-velocity)	(DOP)	(I-energy)	(Weight)	(Total Thickness)	Desirability	
1	6.266	169.689	436.067	1.400	39.032	4072.002	192.283	0.777	Selected
2	10.129	136.425	607.571	6.720	151.219	3347.195	159.025	0.257	

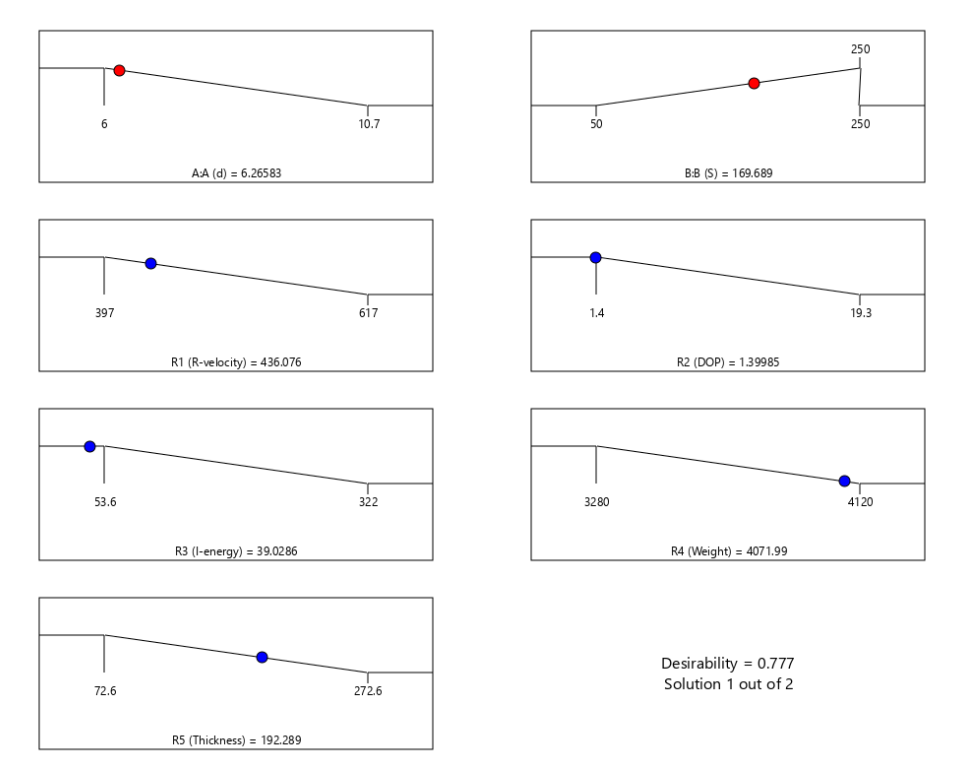


Fig. 11. Optimal numerical solution for optimization variables (\mathbf{r}_{opt}) and (\mathbf{S}_{opt}) .

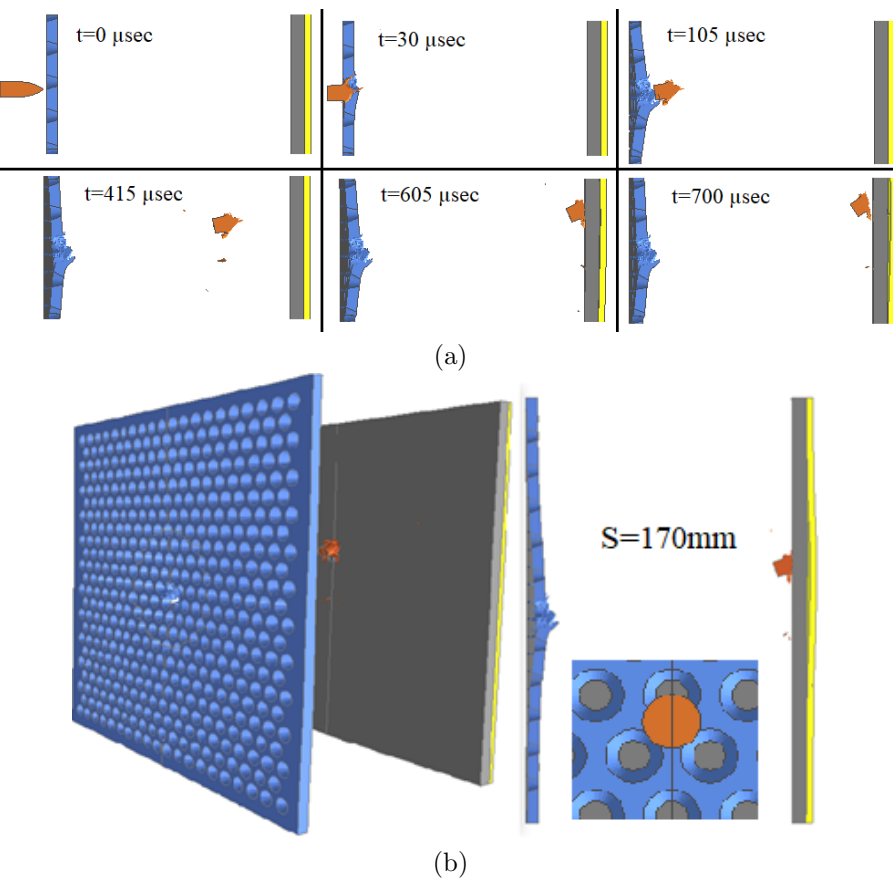


Fig. 12. Numerical solution illustrating the impact on the optimal armor structure using LS-DYNA, considering optimal variables S_{opt} =170mm and r_{opt} =6mm; a): Time events from the bullet's initial strike, deviation, erosion, flight and stopping by the back hybrid composite plate, b): Isometric view of the armor system upon fully stopping the projectile (bullet hit position: side of the hole).

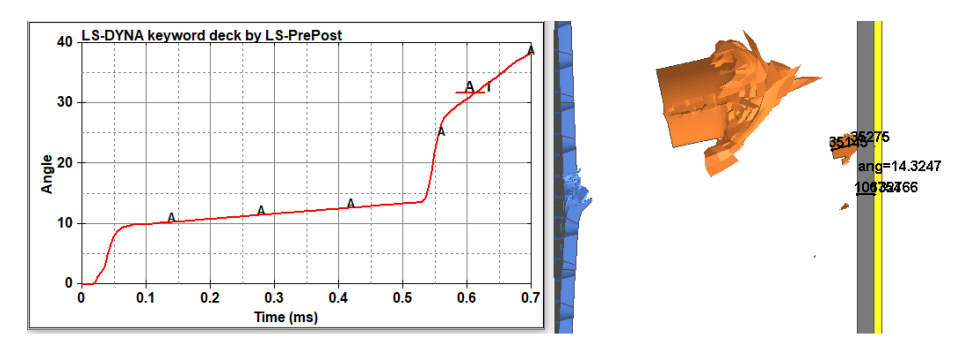


Fig. 13. The curve of the change in the angle of deviation of the bullet during its flight and deformation of bullet (V = 820 m/s) (bullet hit position: side of hole).

Numerical solution for various time steps, illustrating the impact on the optimal armor structure using LS-DYNA, considering optimal variables S_{opt} =170mm and r_{opt} =6mm are shown in Fig. 12. Time events including the bullet's initial strike, deviation, erosion, flight and stopping by the base armor hybrid composite plate are captured. The curve depicting the change in the bullet's deviation angle during its flight including the moments indicated in Fig.12 and the curve of total internal energy absorbed by the base armor reveals that the internal energy absorbed by the armor (sufficient to defeat the bullet) is at its minimum when the moment of impact coincides with the largest angle of deflection of the bullet (Fig. 13).

3.3. Ballistic Performance Study of the Optimal Protection System

To describe the ballistic performance of the optimal protection system obtained in the previous section, the numerical study considers two scenarios. In the first scenario (asymmetric impact), where the impact point was located on the side of the hole, the projectile deviated from its original trajectory after passing through the considered plate, resulting in a reduction of its energy and facilitating the base armor's ability to stop it. Furthermore, the projectile's velocity decreased to 337 m/s after penetrating the perforated plate (Fig. 14).

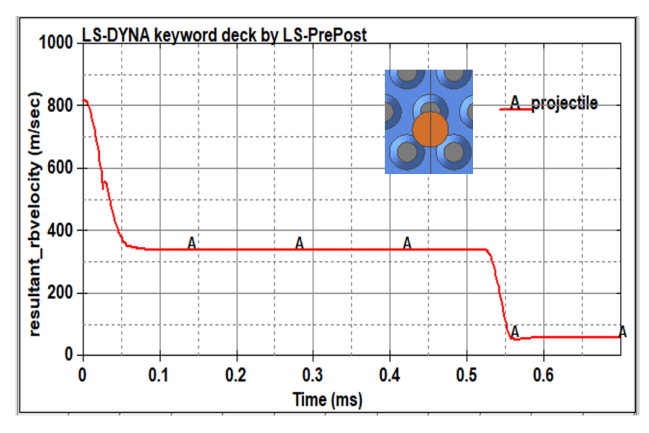


Fig. 14. Bullet velocity curve (bullet hit position: side of hole).

There was also significant deformation and wear on the projectile's tip, and the bullet lost 88% of its kinetic energy after penetrating the perforated plate, as illustrated in Fig. 15. According to this figure, at approximately t=0.53ms, when a sharp deviation occurs in Figs. 13 and 14, the bullet's kinetic energy decreases and approaches zero.

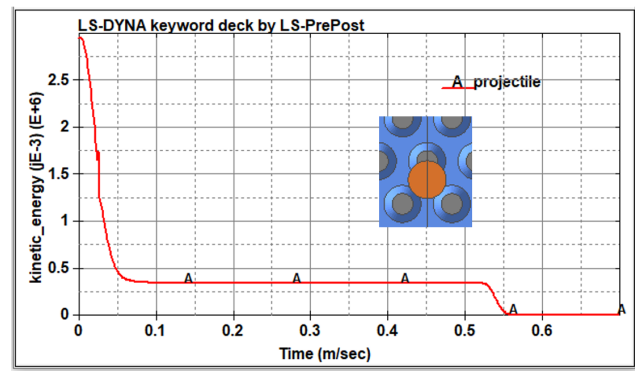


Fig. 15. Kinetic energy curve of bullet (bullet hit position: side of hole).

The perforated plate accounted for 80% of the total internal energy absorbed to stop the projectile, as shown in Fig. 16. This figure indicates that immediately after the bullet first contacts the ceramic layer of the base armor, the remaining kinetic energy of the bullet is absorbed by the ceramic layer, while the energy absorbed by the Kevlar layer is nearly zero and it remains intact.



Fig. 16. Total internal energy curves of each component; (V= 820m/s) (bullet hit position: side of hole).

In the second scenario, where the impact point was considered at the center of the conical hole, the projectile velocity decreased to $554 \,\mathrm{m/s}$ after penetrating the perforated plate (Fig. 17). In this scenario, no deviation angle occurs and after stopping the bullet by the base armor, it rebounds after about $t=0.25 \,\mathrm{ms}$.

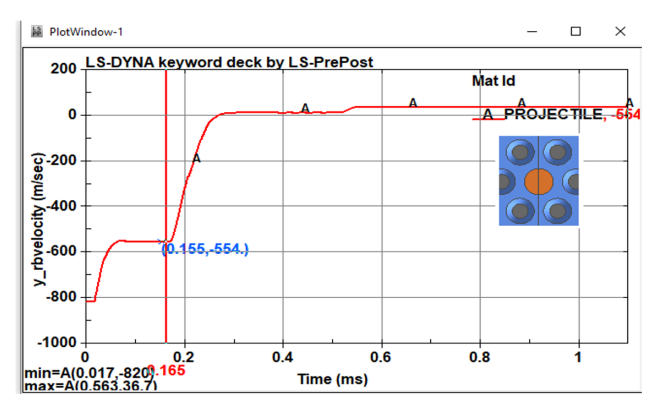


Fig. 17. Bullet velocity curve (bullet hit position: center of hole).

A noticeable deformation of the projectile was observed, with an elongation along the longitudinal axis by 14.2mm. Analysis of the internal energy absorption curves for each component of the protective system revealed that the perforated plate, ceramic layer, and Kevlar layer contributed 64%, 32.8%, and 3%, respectively, to the total absorbed energy (Fig. 18). A comparison between Fig. 18 and Fig. 16 reveals that asymmetric impact, which is statistically more probable than a direct impact at the center of the hole, results in better dissipation of the projectile's kinetic energy. Additionally, in Fig. 16, the Kevlar layer undergoes deformation and the ceramic layer exhibits localized damage, whereas in Fig. 18, the ceramic layer remains nearly intact, as illustrated in Fig. 13.

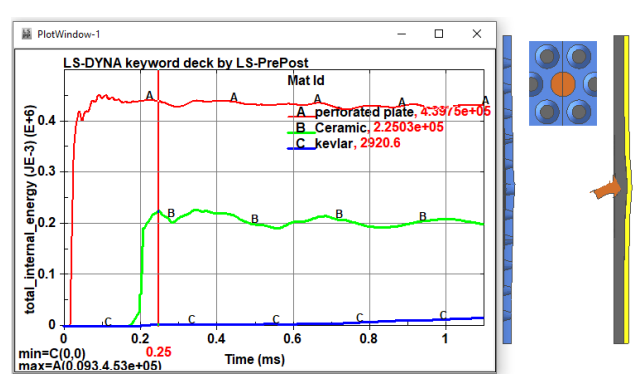


Fig. 18. Total internal energy curves of each component; (V=820m/s) (bullet hit position: center of hole).

The initial analysis revealed that the base armor, when used alone, was inadequate in preventing projectile penetration, resulting in a residual velocity of 204m/s (Fig. 19). This finding underscores the need for an additional protective layer to enhance the system's ballistic resistance.

To overcome this limitation, a perforated armor plate featuring conical holes was positioned in front of the base armor. The integration of this additional armor significantly improved protection while reducing the overall system weight by 30% compared to a solid homogeneous plate. This weight reduction is critical for applications where mobility and maneuverability are key considerations, such as in military vehicles and personal protective equipment.

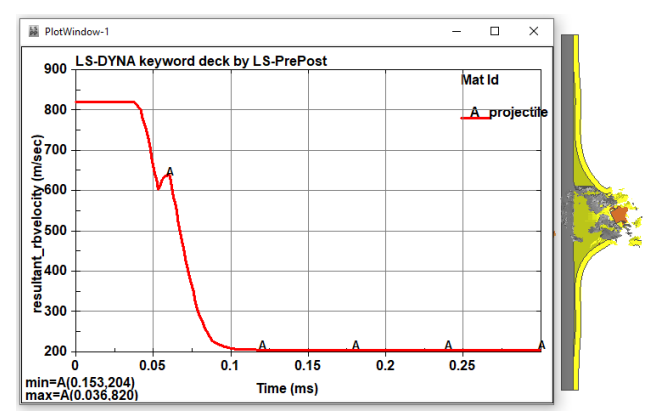


Fig. 19. Numerical ballistic study for base armor (SiC/Kevlar) without perforated plate by LS-DYNA and residual velocity curve of the projectile.

The study also examined the effect of impact location on ballistic performance. When the projectile struck the center of a perforation (a scenario often considered a critical weak point in conventional cylindrical-hole designs), the proposed conical-hole structure demonstrated enhanced energy absorption. The perforated plate absorbed 63% of the total energy dissipated by the protection system, leading to a 54.7% reduction in the projectile's kinetic energy after passing through the perforated plate (Fig. 20). This finding highlights the effectiveness of conical perforations in increasing impact resistance, as opposed to conventional cylindrical holes, which offer lower ballistic resistance under critical impact conditions.

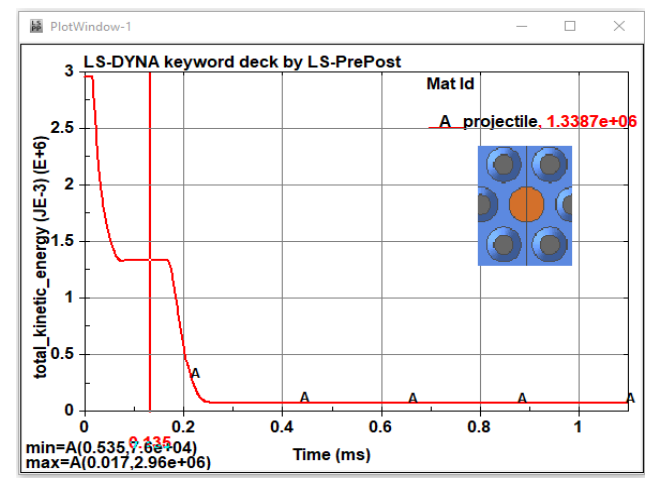


Fig. 20. Kinetic energy curve of the bullet (bullet hit position: center of hole).

4. Conclusions

A numerical study was conducted to assess the ballistic protection offered by a perforated steel plate featuring conical holes, in conjunction with a base armor made of Sic/Kevlar, against a 12.7mm armor-piercing (AP) projectile. The new design was tested under an asymmetric impact scenario (when the projectile strikes the edge of a hole). In this situation, the projectile experienced significant trajectory deviation upon penetrating the perforated plate. Numerical simulations identified optimal values of 170mm for the air spacing and 6mm for the conical hole's minor circle diameter, resulting in a maximum deflection angle of approximately 14 degrees. This deflection was crucial in reducing penetration capability, preventing the projectile from breaching the base armor. In the second scenario, a comparison with previous research shows that conventional perforated plates (featuring cylindrical holes) often fail to maintain effectiveness when the projectile's impact point aligns with the center of a hole. However, the introduction of conical perforations alters the failure mechanism of the projectile, thereby enhancing the overall ballistic performance. The results indicate that the proposed system not only improves resistance to penetration but also modifies the impact dynamics, increasing the likelihood of projectile fragmentation or deflection. Accordingly, the main outcomes concluded from the present study are listed as follows:

- Enhanced energy absorption: The conical perforated plate absorbed 63% of the total dissipated energy, effectively reducing the projectile velocity.
- Weight reduction: A 30% decrease in weight was achieved compared to a homogeneous plate, without compromising ballistic performance.
- Impact location sensitivity: The proposed design significantly enhanced protection under critical impact scenarios, unlike conventional perforated plates.
- Trajectory deviation mechanism: The optimal air spacing of 170 mm and conical hole minor circle diameter of 6 mm induced a projectile deflection angle of 14 degrees, preventing the projectile from penetrating the base armor.

Overall, these findings confirm that the proposed armor configuration provides superior ballistic resistance compared to traditional designs, making it a promising solution for lightweight armor protection against large-caliber threats.

References

- P. Zhang, Z. Wang, P. Zhao, L. Zhang, X. C. Jin, and Y. Xu, "Experimental investigation on ballistic resistance of polyurea coated steel plates subjected to fragment impact," Thin-Walled Struct., vol. 144, p. 106342, 2019.
- [2] S. Balos, V. Grabulov, L. Sidjanin, M. Pantic, and I. Radisavljevic, "Geometry, mechanical properties and mounting of perforated plates for ballistic application," Mater. Des., vol. 31, no. 6, pp. 2916–2924, 2010.
- [3] M. Übeyli, R. O. Yıldırım, and B. Ögel, "On the comparison of the ballistic performance of steel and laminated composite armors," Mater. Des., vol. 28, no. 4, pp. 1257–1262, 2007.
- [4] S. Balos, D. Howard, A. Brezulianu, and D. Labus Zlatanović, "Perforated Plate for Ballistic Protection—A Review," Metals (Basel)., vol. 11, no. 4, p. 526, 2021.
- [5] T. Cui, Q. Qin, W. Yan, T. Wang, and J. Zhang, "Ballistic Resistance of Novel Amorphous-Alloy-Reinforced Perforated Armor," Acta Mech. Solida Sin., vol. 34, no. 1, pp. 12–26, 2021.
- [6] S. Chocron, C. E. Anderson Jr, D. J. Grosch, and C. H. Popelar, "Impact of the 7.62-mm APM2 projectile against the edge of a metallic target" Int. J. Impact Eng., vol. 25, no. 5, pp. 423–437, 2001.
- [7] N. Kılıç, S. Bedir, A. Erdik, B. Ekici, A. Taşdemirci, and M. Güden, "Ballistic behavior of high hardness perforated armor plates against 7.62 mm armor piercing projectile," Mater. Des., vol. 63, pp. 427–438, 2014.
- [8] I. Radisavljevic, S. Balos, M. Nikacevic, and L. Sidjanin, "Optimization of geometrical characteristics of perforated plates," Mater. Des., vol. 49, pp. 81–89, 2013.
- [9] A. Mubashar, E. Uddin, S. Anwar, N. Arif, S. Waheed Ul Haq, and M. A. K. Chowdhury, "Ballistic response of 12.7 mm armour piercing projectile against perforated armour developed from structural steel," Proc. Inst. Mech. Eng. Part L J. Mater. Des. Appl., vol. 233, no. 10, pp. 1993–2005, 2019.
- [10] W. Hao, P. Zhang, J. Xie, M. Hou, Z. Wang, and X. Bai, "Investigation of impact performance of perforated plates and effects of the perforation arrangement and shape on failure mode," Eng. Fail. Anal., vol. 140, p. 106638, 2022.

- [11] A. Shi, X. Hong, H. Han, K. Xia, X. Fan, C. Qin and S. Sun, "Research on ballistic protection characteristics of perforated plates made of different steel materials for 12.7 mm penetrator projectile," J. of Physics: Conference Series, IOP Publishing, 2024, p. 12007.
- [12] D. Acar, B. H. Canpolat, and Ö. N. Cora, "Ballistic performances of Ramor 500, Armox Advance and Hardox 450 steels under monolithic, double-layered, and perforated conditions," Eng. Sci. Technol. an Int. J., vol. 51, p. 101653, 2024.
- [13] M. H. M. Alawsi, A. M. A. Al-Zobaede, and S. M. A. Al-Obaidi, "Experimental and Numerical Study of Ballistic Impact Performance on Steel Plate Structures," J. Eng. Sustain. Dev., vol. 29, no. 2, pp. 177–183, 2025.
- [14] N. Kılıç, B. Ekici, and S. Bedir, "Optimization of high hardness perforated steel armor plates using finite element and response surface methods," Mech. Adv. Mater. Struct., vol. 24, no. 7, pp. 615– 624, 2017.
- [15] P. J. Hazell, Armour: materials, theory, and design. CRC press, 2022.
- [16] N. Djordjevic et al., "Modelling of shock waves in fcc and bcc metals using a combined continuum and dislocation kinetic approach," Int. J. Plast., vol. 105, pp. 211–224, 2018.
- [17] P. L. N. Fernando, D. Mohotti, and A. Remennikov, "Behaviour of explosively welded impedance-graded multi-metal composite plates

- under near-field blast loads," Int. J. Mech. Sci., vol. 163, p. 105124, 2019.
- [18] A. Kyner, K. Dharmasena, K. Williams, V. Deshpande, and H. N. G. Wadley, "High intensity impact of granular matter with edge-clamped ductile plates," Int. J. Impact Eng., vol. 111, pp. 106–129, 2018.
- [19] G. R. Johnson, "A constitutive model and data for metals subjected to large strains, high strain rates and high temperatures," in Proceedings of the 7th International Symposium on Ballistics, The Hague, Netherlands, 1983, 1983.
- [20] Y. K. Xiao, H. Wu, Q. Fang, W. Zhang, and X. Z. Kong, "Hemispherical nosed steel projectile highspeed penetration into aluminum target," Mater. Des., vol. 133, pp. 237–254, 2017.
- [21] J. Cao, J. Lai, J. Zhou, N. Kang, L. Du, and Y. Miao, "Experiments and simulations of the ballistic response of ceramic composite armors," J. Mech. Sci. Technol., vol. 34, pp. 2783–2793, 2020.
- [22] P. Hu, Y. Cheng, P. Zhang, J. Liu, H. Yang, and J. Chen, "A metal/UHMWPE/SiC multi-layered composite armor against ballistic impact of flatnosed projectile," Ceram. Int., vol. 47, no. 16, pp. 22497–22513, 2021.
- [23] W. Burian, J. Marcisz, L. Starczewski, and M. Wnuk, "A probabilistic model of optimising perforated high-strength steel sheet assemblies for impact-resistant armour systems," Probl. Mechatroniki Uzbroj. lotnictwo, inżynieria bezpieczeństwa, vol. 8, 2017.